

Structurally embedded reflectors and mirrors for elastic wave focusing and energy harvesting

S. Tol, F. L. Degertekin, and A. Erturk^{a)}

G. W. Woodruff School of Mechanical Engineering, Georgia Institute of Technology, Atlanta, Georgia 30332, USA

(Received 8 March 2017; accepted 7 October 2017; published online 24 October 2017)

The harvesting of elastic waves propagating in structures can be enhanced dramatically via spatial focusing using mirror and lens concepts. Recent efforts on the mirror design have employed cylindrical stubs that form elliptical and parabolic geometries to focus structure-borne waves originating from a point source and incident plane waves, respectively. In those first-generation heuristic efforts, bulky cylindrical attachments served as effective reflectors while drastically altering thin host structures. Enabling structurally embedded mirror (SEM) configurations that avoid substantial modification of the host system requires a thorough understanding of the elastic mirror dynamics. This work presents a detailed investigation of SEM design, analysis, and experimental validation for enhanced elastic wave energy harvesting, among other applications that can benefit from spatially focused wave intensity. The SEM concept proposed in this effort uses metallic spheres (e.g., tungsten, lead, and steel) inserted into blind holes in a flat aluminum plate domain. The results show that, while SEM performance improves with property mismatch between the inclusion and the host materials, transmission resonances of the inclusions are detrimental to reflection performance and have to be avoided. A relationship between elastic mirror geometry and wavelength is unveiled to minimize the energy concentration in the side lobes around the intended focus, enabling small-sized and simple harvester design. These basic concepts and principles, demonstrated through finite-element simulations, are validated experimentally over a range of frequencies. Dramatic enhancement of the harvested power (by an order of magnitude) is also demonstrated using an elliptical SEM made from spherical tungsten inclusions in an aluminum plate. The case of a perforated mirror is also addressed briefly. *Published by AIP Publishing.* <https://doi.org/10.1063/1.5008724>

I. INTRODUCTION

Various methods of vibration/motion energy harvesting have been researched toward enabling next-generation self-powered electronic devices for wireless applications ranging from structural health monitoring to wearable electronic components.^{1–3} The energy conversion methods that have been explored for transforming mechanical (mostly vibrational and kinetic) energy into electricity are the piezoelectric,^{1,2} electromagnetic,^{4,5} electrostatic,^{6,7} and magnetostrictive⁸ conversion techniques, as well as the use of electroactive polymers, such as dielectric elastomers⁹ and ionic polymer-metal composites,^{10,11} polymer electrets,¹² and even gradient effects^{13,14} in elastic dielectrics at submicron thickness levels. Among these alternatives, piezoelectric transduction has received arguably the greatest attention due to the high power density and ease of application piezoelectric materials and their relatively mature fabrication techniques at different geometric scales.¹⁵

The harvesting of standing waves and vibrations has been extensively researched^{1–3} through the use of linear and nonlinear energy harvesters, such as cantilevers with piezoelectric layers undergoing base excitation. However, the available energy of waves traveling in fluids and structures, i.e., propagating acoustic and elastic waves, and the overall

wave propagation approach to the energy harvesting problem have received much less attention, yielding rather limited literature.^{16–28} The wave approach provides new insights for the enhancement of mechanical-to-electrical energy conversion efficiency by spatial localization or focusing wave energy through the use of concepts from metamaterials and phononic crystals.^{16–28} In this context, recently, elastic mirror^{22–24} and phononic crystals lens^{27,28} designs have been implemented for the focusing and enhanced harvesting of structure-borne elastic waves (namely, the lowest antisymmetric Lamb wave mode). Specifically, the elastic mirrors employed in the first-generation configurations^{22–24} were not only heuristic but also their bulky stub extensions (10 times thicker than the host plate) that formed the mirror may not be applicable in many scenarios that require preserving the flat and thin host structure. Furthermore, it was observed that the side lobes near the geometric focus contained significant energy levels. Consequently, patterned segmentation of the piezoelectric domain was employed²⁴ through a wavenumber transformation procedure to harvest the energy at the side lobes.

In order to enable embedded mirror structures beyond heuristic designs by avoiding substantial modification of the host structure and complex segmented harvesters, it is required to have an extensive understanding of the wave focusing performance of these elastic wave mirrors as well as the dynamics of structurally embedded reflectors. In the

^{a)}Author to whom correspondence should be addressed: alper.erturk@me.gatech.edu.

following, first we unveil a basic relationship between the mirror geometry and wavelength of the lowest antisymmetric Lamb wave mode (A_0 mode) in a plate with respect to formation and minimization of the neighboring side lobes observed in previous work.^{22–24} We then investigate the reflection coefficient for reflectors formed by inserting metallic spheres (e.g., tungsten, lead, and steel) into blind holes in a flat aluminum plate domain. The frequency dependence of the reflection coefficient for spherical inclusions of tungsten, lead, and steel in aluminum is reported and its impact on structurally embedded mirror (SEM) performance is discussed. Finally, experimental results are presented for an elliptical SEM using tungsten inclusions in an aluminum plate to verify the simulations and explore the energy harvesting performance enhancement. The perforated mirror scenario (mass subtraction rather than inclusion) via through holes is also addressed briefly.

II. MIRROR GEOMETRY AND WAVELENGTH CONSIDERATIONS

First, the impact of mirror geometry on the focusing performance and hence the harvester design are investigated through finite element simulations of both elliptical and parabolic mirrors in COMSOL Multiphysics® (note that finite-element modeling of guided elastic waves is not the main scope of this work and there exists a vast literature^{29,30} on

that topic). The numerical results, summarized in Figs. 1 and 2, reveal a simple recipe for design of elliptical and parabolic elastic wave mirrors, respectively. Figure 1(a) shows the elliptical mirror design, where a is the semi-major axis length, b is the semi-minor axis length, and f is the distance to the focal point from the center of the semi-ellipse (hence, $f^2 = a^2 - b^2$). It is useful to define another geometric parameter, $d = a - f$, which is the distance between the focus and the edge of the mirror in Fig. 1(a). Figures 1(b)–1(d) show the out-of-plane RMS (root-mean-square) velocity wave field when elastic waves generated by a point source at the other focus of the semi-ellipse (not shown in the figure) are concentrated at the focus of SEMs with the same aperture (i.e., minor axis) length ($2b$), but different focal points, namely, the cases of $d = 3\lambda/4$, $d = \lambda$, and $d = 5\lambda/4$ (where λ is the wavelength). In the simulations, an elastic mirror of 120 mm minor-axis length was formed by embedding 3 mm diameter spherical inclusions into blind holes with 3.5 mm center-to-center spacing in the form of a semi-ellipse in a 914 mm × 914 mm aluminum plate domain of 3.175 mm thickness (the gaps in the blind holes of spherical inclusions were filled with epoxy). A sinusoidal burst excitation with a center frequency of 50 kHz was applied as the point source (note that $\lambda = 23.5$ mm at 50 kHz, which is an A_0 mode Lamb wave). This design frequency was selected as in our previous work^{22–24,27,28} to have practical dimensions in the experimental setup. Second-order tetrahedral mesh elements

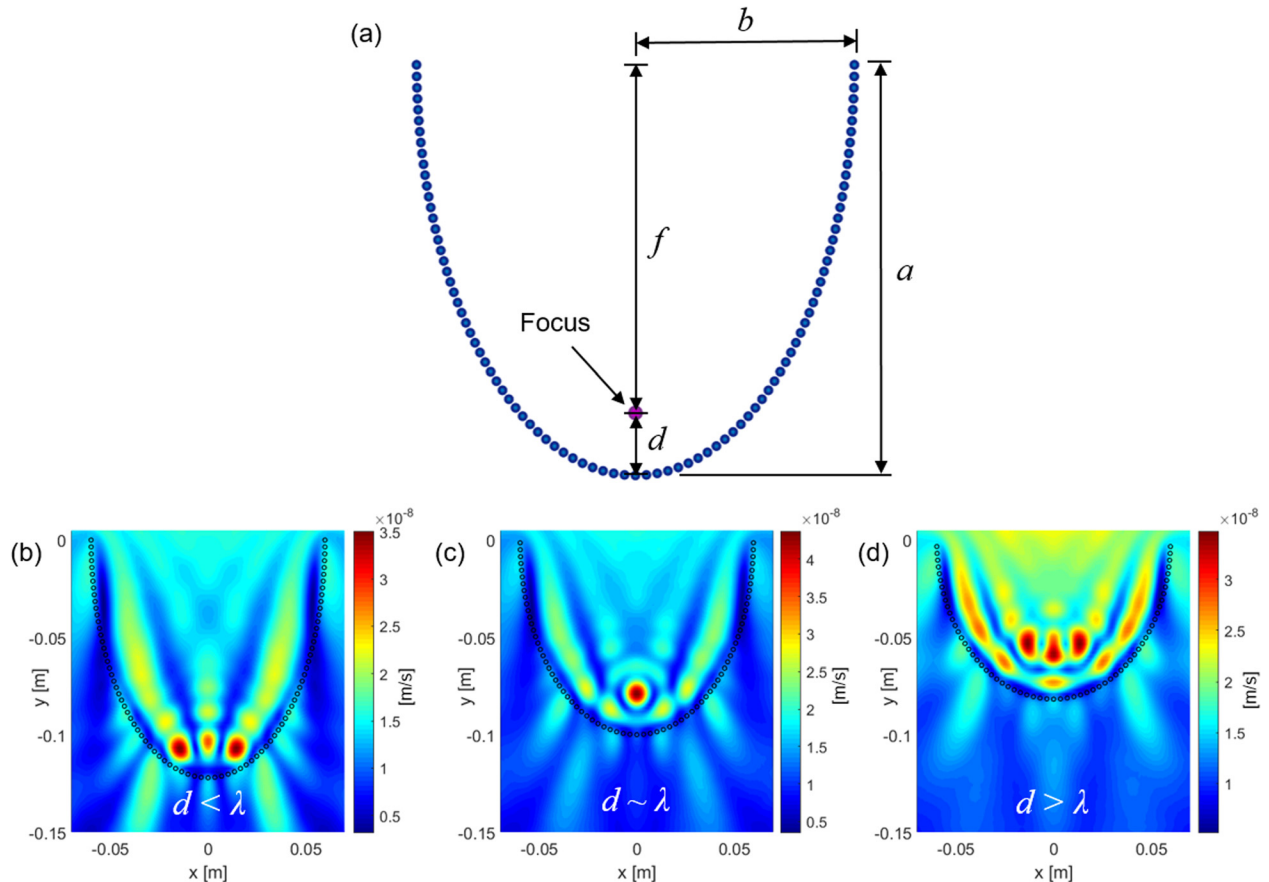


FIG. 1. (a) Schematic and geometric parameters of the elliptical SEM design made from spherical inclusions and (b)–(d) wavelength-geometry relationship revealing ideal focusing for $d \sim \lambda$. Numerical simulation of the out-of-plane RMS velocity wave field for (b) $d = 3\lambda/4$, (c) $d \sim \lambda$, and (d) $d = 5\lambda/4$. Side lobes are significantly pronounced for $d < \lambda$ and $d > \lambda$ and are rather negligible for $d \sim \lambda$.

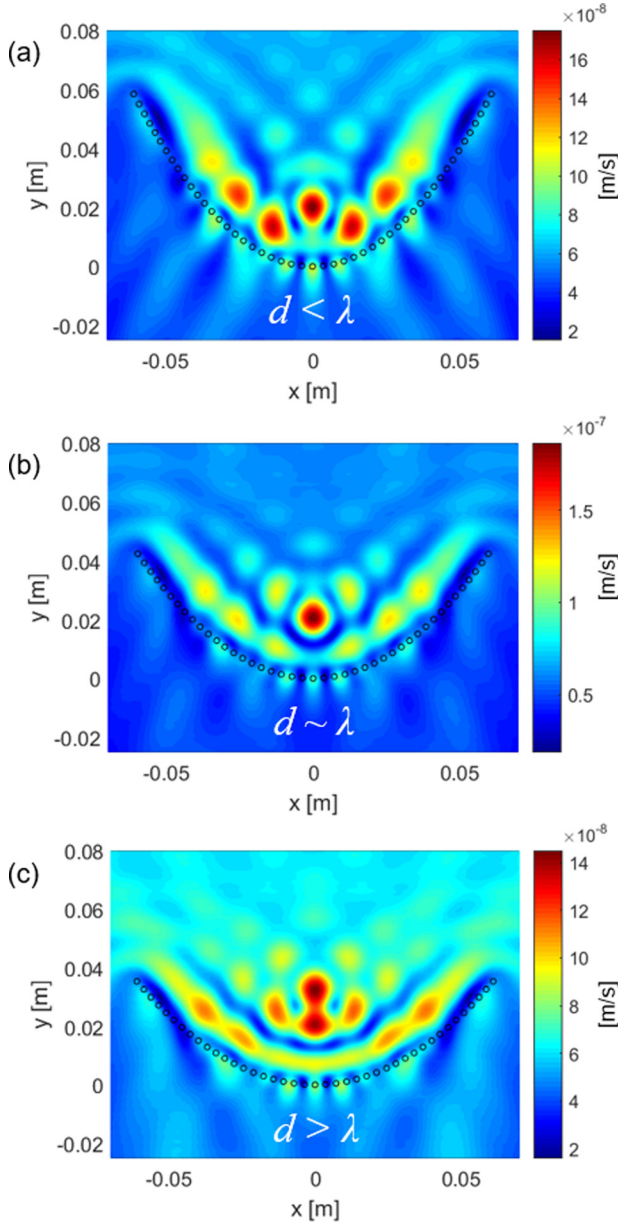


FIG. 2. Parabolic SEM wavelength-geometry relationship revealing ideal focusing for $d \sim \lambda$. Numerical simulation of the out-of-plane RMS wave field for (a) $d = 3\lambda/4$, (b) $d \sim \lambda$, and (c) $d = 5\lambda/4$. Side lobes are significantly pronounced for $d < \lambda$ and $d > \lambda$ and are rather negligible for $d \sim \lambda$.

(with 10 nodes per element) were used in the simulations. The mesh size was set to satisfy 7 mesh elements per wavelength (so that the wave was equally resolved in space) and a Courant-Friedrichs-Lowy number of ~ 0.2 was used to set the time step. The out-of-plane velocity wave fields were obtained using time-domain analysis. As can be observed in Figs. 1(b)–1(d), the side lobes near the focal point have significant energy when the distance d is greater or smaller than the wavelength λ . On the other hand, the side lobes become negligible when the mirror is designed to have a d value that is equal to λ . This observation, supported by simulations over a range of d values, leads to a criterion that the ideal elastic wave mirror with minimal (or negligible) side lobes should have $d \sim \lambda$ (roughly $d = \lambda \pm 0.1 \lambda$). Remarkably, other than the elliptical mirror scenario (which is the main focus

of the case studies in this paper), Fig. 2 shows similar results for the parabolic mirror case as well. Therefore, when designing a parabolic SEM to focus incident plane waves at a given frequency, one should again choose $d \sim \lambda$ (as the geometry-wavelength design criterion) in order to reduce the energy of side lobes. This criterion has a direct impact on the harvester design since a smaller piezoelectric patch with a single electrode can be used instead of a larger transducer with a complex harvester/electrode pattern and wiring.²⁴

III. REFLECTION COEFFICIENT AND FREQUENCY CONSIDERATIONS

The intensity of elastic wave reflection from the inclusions forming the mirror is another critical factor in SEM performance. In addition to the material property mismatch, one should also consider the finite size of the inclusions leading to frequency dependent reflectivity. This is investigated through finite-element simulation of A_0 mode Lamb wave reflection and transmission in a simplified aluminum waveguide where the reflector is formed by a spherical inclusion in a cylindrical blind hole [Fig. 3(a)]. While it is depicted as a one-dimensional waveguide in Fig. 3(a), by applying periodic boundary conditions on the sides [in the y -direction in Fig. 3(a)] of this waveguide, a laterally infinite plate with periodic spherical inclusions is constructed to explore plane wave propagation in the x -direction with a focus on the reflection from the inclusions. The time-domain response to incident plane wave excitation is solved for burst excitations with different center frequencies. From the ratio of the Fourier transforms of the reflected and the incident wave packets, the reflection coefficient is calculated for different frequencies. Figure 3(b) shows the resulting reflection coefficient frequency response (based on out-of-plane velocity magnitude) for a 3 mm diameter spherical inclusion with 3.5 mm (center-to-center spacing of the inclusions in the mirror designs) lateral periodicity in the 3.175 mm thick aluminum plate simulated by time-domain analysis for tungsten, lead, and steel spheres embedded in otherwise epoxy filled blind holes. It is observed that, at very low frequencies, the reflection coefficient is very low since the wavelength is much larger than the inclusion size (hence, the inclusion is not visible to the wave). The trend in the reflection coefficient with increased frequency is not monotonic. For the frequency range shown in Fig. 3(b), tungsten and steel inclusions result in a single frequency of almost zero reflection, while the lead inclusion yields multiple such frequencies. A careful investigation reveals that these are the transmission resonances (TRs) of the inclusions that lead to almost perfect wave transmission, compatible with the flexural nature of the A_0 mode Lamb wave (see the arrows indicating the rotation of the tungsten sphere at 137 kHz in Fig. 3(c) as an example). The first resonances of these spherical inclusions occur at 137 kHz, 162 kHz, and 175 kHz for tungsten, steel, and lead, respectively, indicating that one should avoid transmission resonances for SEM implementation as the mirror reflection would be poor (these resonances can be captured via local finite-element modeling^{31,32}). We consider the first peak neighborhood of all inclusion

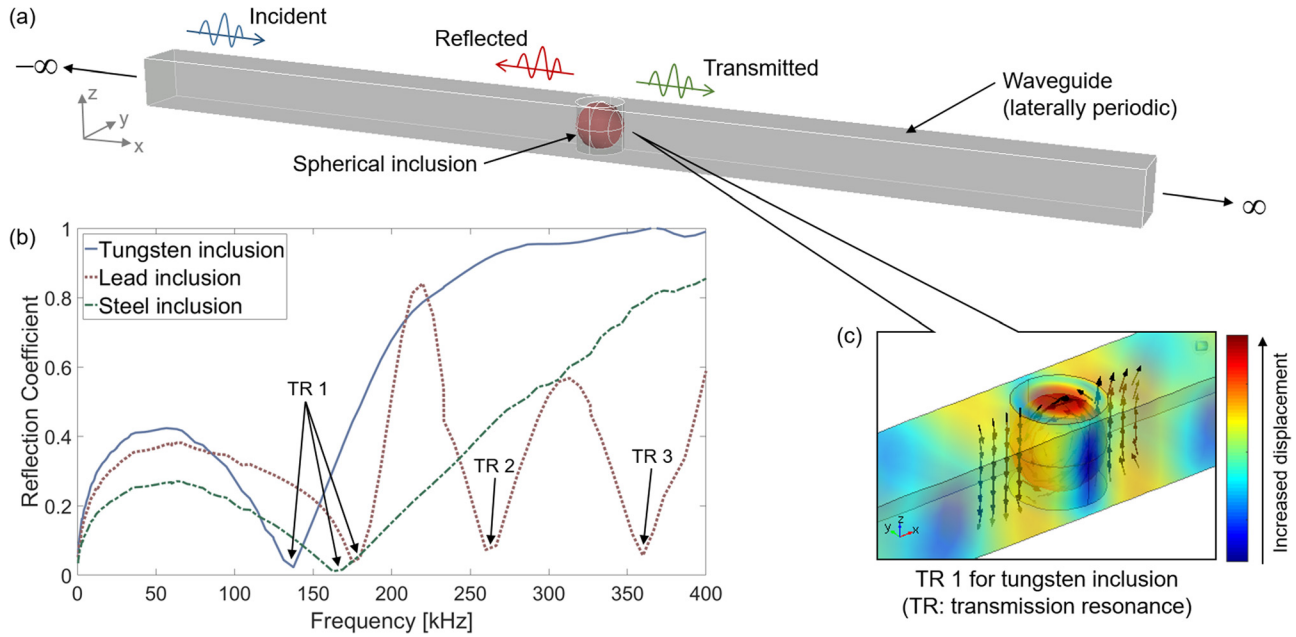


FIG. 3. (a) Laterally periodic waveguide with a spherical inclusion showing the incident, transmitted, and reflected wave components (the waveguide is aluminum, while the inclusion in the cylindrical blind hole is tungsten, lead, or steel); (b) Reflection coefficient for different materials embedded in aluminum exhibiting transmission resonances (denoted by TR) yielding almost zero reflection (which must be avoided in mirror design); (c) Close-up view of the first transmission resonance for a tungsten inclusion (arrows indicate the direction of motion compatible with the A_0 mode).

materials, which is around 50 kHz (where the reflection levels are dominated by the mass effect of the inclusions) to assess the performance of SEM configurations for these different inclusion materials. If one makes geometrically identical mirrors using identical size inclusions of these materials in an aluminum plate, it can be expected that the amplitude at the focus should scale with the reflection coefficient at the design frequency (50 kHz). This is explored next through finite-element simulations of the transient wave field with parameters similar to those of Fig. 1(c).

Figure 4 shows the RMS wave fields of geometrically identical SEM configurations made from spherical tungsten, lead, and steel inclusions of the aforementioned dimensions embedded in aluminum simulated at the design frequency of 50 kHz. The mirrors for all cases in Fig. 4 have $d \sim \lambda$ [Fig. 1(a)] to eliminate side lobes. For the same excitation source (i.e., identical intensity), as expected, the RMS values at the mirror focus are proportional to the values of the reflection coefficients at this frequency (i.e., the order of reflection coefficient values at 50 kHz in Fig. 3(b) is in agreement with the order of focusing intensities in Fig. 4).

IV. EXPERIMENTAL VALIDATION AND ENERGY HARVESTING RESULTS

A. Experimental setup

Experimental validation of SEM simulations was performed using the setup shown in Fig. 5(a). This figure also shows the fabricated SEM and three piezoelectric attachments (two harvesters—baseline and SEM—and one source). A close-up view of the SEM is displayed in Fig. 5(b). The source piezoelectric patch was excited by 4 cycles of sinusoidal burst at desired frequencies using a function generator and a voltage amplifier. A scanning Laser Doppler

Vibrometer (LDV) was used to measure the resulting wave field by recording the out-of-plane velocity of the plate over a grid of points covering the mirror domain [back of the view shown in Fig. 5(a) inset]. With proper triggering of the LDV measurements, the wave field was reconstructed. The RMS values were obtained by integrating the measured response over time.

B. Wave field validation

First, in the absence of piezoelectric energy harvester patches, the overall out-of-plane velocity field was measured over a broad range of excitation frequencies to explore the frequency dependence of the RMS wave field. Since the SEM in Fig. 5(b) was designed for a specific frequency (50 kHz), side lobes are expected (according to Fig. 1) as one deviates from this excitation frequency. Figure 6 shows experimental RMS out-of-plane velocity field for excitation at various frequencies (from 30 to 70 kHz) centered around the design frequency of 50 kHz and reveals excellent agreement with finite-element simulations. Because the wavelength criterion for ideal focusing [$d \sim \lambda$ in Fig. 1(a)] is not satisfied at frequencies other than the design frequency of 50 kHz, significant side lobes are observed away from this frequency, especially at 30 kHz ($d/\lambda = 0.73$) and 70 kHz ($d/\lambda = 1.15$).

C. Energy harvesting results

Having validated the fabricated SEM design and its focusing performance experimentally, energy harvesting performance enhancement associated with the SEM concept is discussed next. As shown in Fig. 5(a), identical piezoelectric energy harvester disks were bonded at the focus of the SEM and also in a baseline setting at the same distance from the

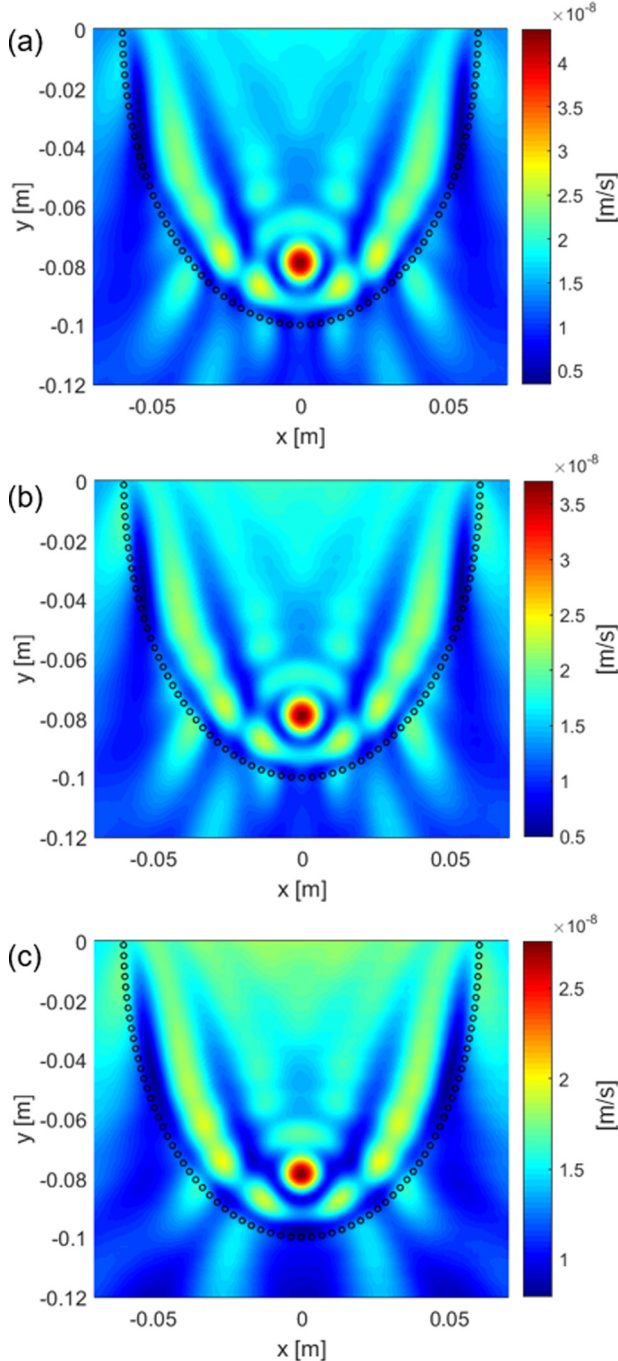


FIG. 4. RMS wave fields of geometrically identical SEM configurations with spherical inclusions made of (a) tungsten (17800 kg/m^3 , 360 GPa), (b) lead (11340 kg/m^3 , 16.1 GPa), and (c) steel (7810 kg/m^3 , 210 GPa) embedded with epoxy filling (1150 kg/m^3 , 2 GPa) into the blind holes in the aluminum plate (2700 kg/m^3 , 70 GPa). Tungsten inclusion yields the largest focusing intensity under the same excitation.

excitation source in the uniform plate region. These two 0.6-mm-thick piezoelectric disks with the half-wavelength diameter (for the design frequency of 50 kHz) were attached to the aluminum plate by means of a vacuum bonding technique using high-shear strength epoxy. Energy harvesting experiments were performed via resistor sweep tests by shunting the bottom and top electrodes of the piezoelectric harvesters to a decade box for a range of resistive electrical loads covering the optimal conditions of both the harvester

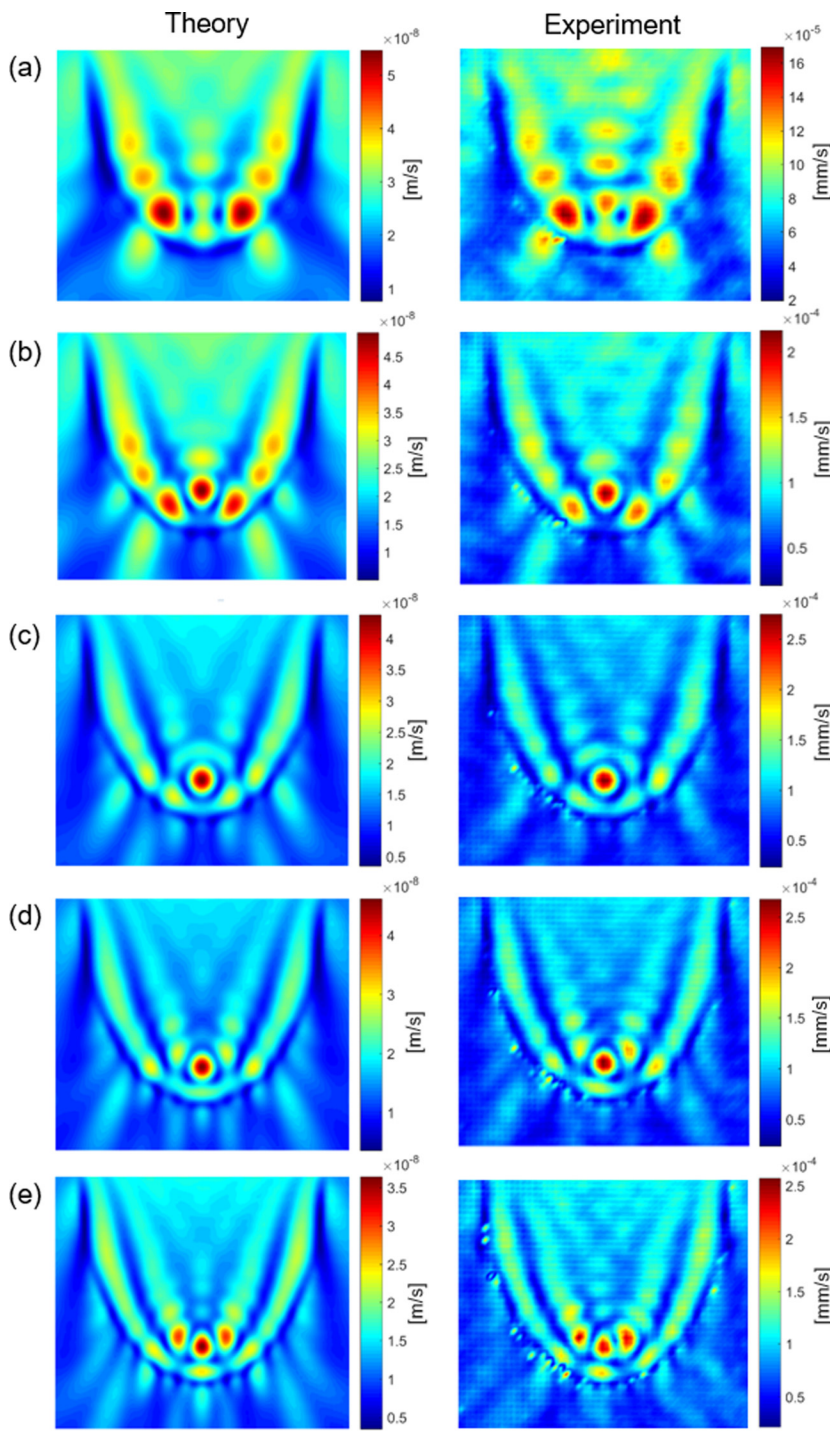
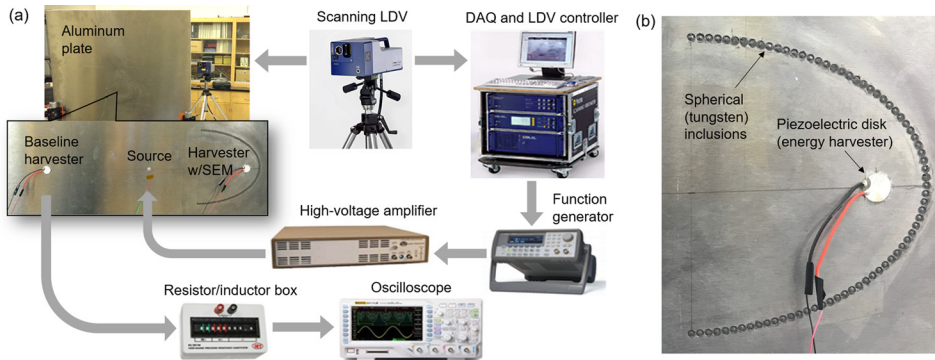
with SEM and the baseline harvester. The average power outputs of the harvesters were calculated from the voltage measurements across the resistor with an oscilloscope. For purely resistive loading, the voltage response waveforms under the 1250Ω optimal load resistance (which is roughly $1/(\omega C_p)$ where ω is the excitation frequency and C_p is the piezoelectric capacitance) are displayed in Fig. 7(a). The average power output data (versus load resistance) were obtained from the RMS of the voltage waveforms as illustrated in Fig. 7(b). Under the same excitation applied to both harvesters, the harvested power is increased by an order of magnitude (~ 11 times) by focusing the elastic waves in the SEM domain as compared to the baseline case of harvesting incident plane waves using an identical piezoelectric disk without SEM. The order of magnitude increase in the power output via SEM (with tungsten inclusion) was also confirmed numerically by comparing the respective SEM finite-element simulation [Fig. 4(a)] with the RMS wave field simulation for the baseline flat plate (not shown here) at the same distance from the source. The square of the RMS wave intensity at the harvester location is ~ 11 times that of the baseline case, in excellent agreement with the results of energy harvesting experiments. The electrical power output can be improved by complex load impedance matching.²¹ For instance, under resistive-inductive loading with the optimal resistor and inductor combination ($8 \text{ k}\Omega$ and 4 mH), the voltage output is increased substantially (by a factor of ~ 4) as compared to purely resistive loading [Fig. 7(c)].

V. PERFORATED MIRROR CASE

An intriguing scenario is to create a large impedance mismatch to improve reflection by using through holes instead of blind holes with metallic inclusions to form the mirror. When a one-dimensional reflection coefficient analysis is performed for an array of through holes (in the same vein as Fig. 3), one obtains the solid black curve in Fig. 8(a), where SEM with metallic inclusion cases from Fig. 3(b) is also shown for comparison. The reflection coefficient makes a peak at a relatively low frequency (around 10–15 kHz), which could be of interest to enable low-frequency mirrors to match the frequency content of typical ambient energy. However, the reflection coefficient resulting from the through hole is rather low; as a result, a perforated mirror made using through holes yields much lower intensity [at the focus point as shown in Fig. 8(b)] as compared to Fig. 4 cases. Overall, there will always be a gain in the presence of a properly designed mirror setting (as compared to the baseline case of a flat plate); however, the gain strongly depends on the reflection coefficient of the inclusion. Therefore, in order to enable low-frequency mirrors without increasing the size, a more plausible way would be to exploit bandgap formation via locally resonant metamaterials^{33–35} at low frequencies.

VI. CONCLUSIONS

An experimentally validated structurally embedded mirror (SEM) design methodology was presented for enhanced elastic wave energy focusing and harvesting, among other



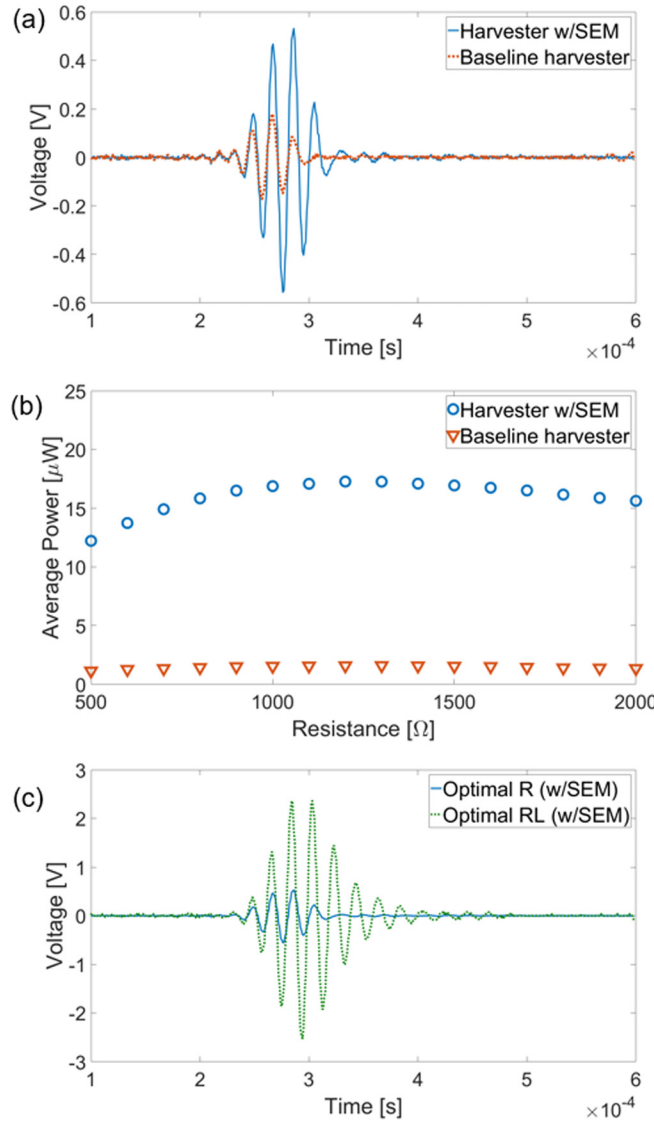


FIG. 7. (a) Comparison of voltage output histories of the harvester with SEM and the baseline harvester for optimal resistive loading (1250Ω); (b) Comparison of average power output data for a range of resistive electrical loads; (c) Further performance enhancement by resistive-inductive loading ($8 \text{k}\Omega$, 4mH) for the harvester with SEM. Results were obtained under 4-cycle sinusoidal burst excitation at 50kHz .

applications that can benefit from spatially focused wave intensity. The SEM configuration proposed in this effort was enabled by inserting metallic spheres (heavier than host structure) into blind holes that form the mirror geometry in the flat plate domain. The relationship between SEM geometry and wavelength was unveiled in order to eliminate or minimize the formation of side lobes near the focus so that a small-sized harvester can be used conveniently at the focus (without the complexity of harvester/electrode segmentation and associated wiring). The correlation between SEM focusing performance and reflection coefficient of embedded spherical inclusions was shown, and the importance of inclusion-related transmission resonances was discussed (such frequencies have to be avoided for enhanced reflection). Dramatic enhancement of the harvested power by more than an order of magnitude (as compared to the baseline case) was also demonstrated experimentally by using an

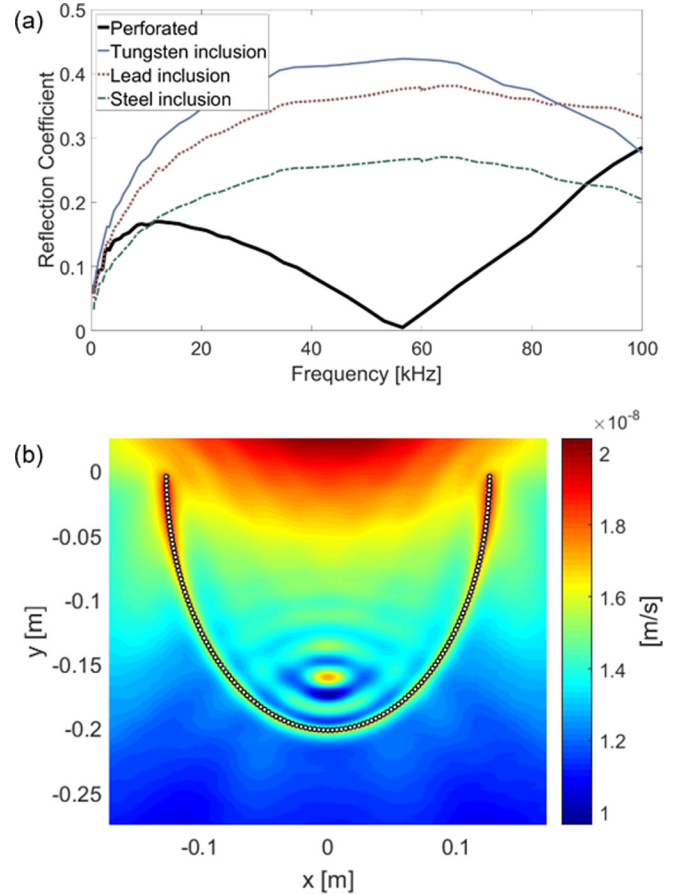


FIG. 8. (a) Reflection coefficient frequency response for through hole (perforated) inclusion in a one-dimensional waveguide compared with SEM cases (previously described with Fig. 3); and (b) RMS wave field for a perforated mirror at 15 kHz [which is the vicinity of optimal reflection according to (a)] yielding focusing with very low intensity (cf. Fig. 4 cases of SEM).

elliptical SEM that employed spherical tungsten inclusions in an aluminum plate. Finite-element simulations showed excellent agreement with experimental measurements, validating the SEM design criterion and focusing performance. The case of a perforated mirror was also addressed by replacing the inclusions with through holes (in the sense of mass subtraction to create a large impedance mismatch). A low-frequency, low-intensity peak was observed in the reflection coefficient of the through hole case, yielding a low gain in the focused energy. While there will always be a gain in the presence of a properly designed mirror setting (as compared to the baseline case of a flat plate), the gain strongly depends on the reflection coefficient of the inclusion. Therefore, it is suggested that a more plausible way to enable low-frequency mirrors could be to exploit bandgap formation via locally resonant metamaterials, which is of interest for future work.

ACKNOWLEDGMENTS

This work was supported in part by the National Science Foundation under Grant No. CMMI-1333978, which is gratefully acknowledged. The authors would also like to thank Dr. Massimo Ruzzene for making the scanning LDV system available.

- ¹S. Roundy, P. K. Wright, and J. M. Rabaey, *Energy Scavenging for Wireless Sensor Networks with Special Focus on Vibrations* (Springer, New York, 2004).
- ²A. Erturk and D. J. Inman, *Piezoelectric Energy Harvesting* (Wiley, 2011).
- ³N. Elvin and A. Erturk, *Advances in Energy Harvesting Methods* (Springer, 2013).
- ⁴C. B. Williams and R. B. Yates, *Sens. Actuators, A* **52**(1-3), 8–11 (1996).
- ⁵P. Glynne-Jones, M. J. Tudor, S. P. Beeby, and N. M. White, *Sens. Actuators A* **110**(1-3), 344–349 (2004).
- ⁶P. D. Mitcheson, P. Miao, B. H. Stark, E. Yeatman, A. Holmes, and T. Green, *Sens. Actuators A* **115**(2), 523–529 (2004).
- ⁷L. G. W. Tvedt, D. S. Nguyen, and E. Halvorsen, *Microelectromech. Syst., J.* **19**(2), 305–316 (2010).
- ⁸L. Wang and F. Yuan, *Smart Mater. Struct.* **17**, 045009 (2008).
- ⁹R. D. Kornbluh, R. Pelrine, H. Prahlad, A. Wong-Foy, B. McCoy, S. Kim, J. Eckerle, and T. Low, *MRS Bull.* **37**(3), 246–253 (2012).
- ¹⁰R. Tiwari, K. J. Kim, and S. M. Kim, *Smart Struct. Syst.* **4**(5), 549–563 (2008).
- ¹¹M. Aureli, C. Prince, M. Porfiri, and S. D. Peterson, *Smart Mater. Struct.* **19**(1), 015003 (2010).
- ¹²S. Anton, K. Farinholt, and A. Erturk, *J. Intell. Mater. Syst. Struct.* **25**(14), 1681–1692 (2014).
- ¹³Q. Deng, M. Kammoun, A. Erturk, and P. Sharma, *Int. J. Solids Struct.* **51**(18), 3218–3225 (2014).
- ¹⁴A. G. Moura and A. Erturk, *J. Appl. Phys.* **121**(6), 064110 (2017).
- ¹⁵K. Cook-Chennault, N. Thambi, and A. Sastry, *Smart Mater. Struct.* **17**(4), 043001 (2008).
- ¹⁶L. Y. Wu, L. W. Chen, and C. M. Liu, *Appl. Phys. Lett.* **95**(1), 013506 (2009).
- ¹⁷S. Gonella, A. C. To, and W. K. Liu, *J. Mech. Phys. Solids* **57**(3), 621–633 (2009).
- ¹⁸W. C. Wang, L. Y. Wu, L. W. Chen, and C. M. Liu, *Smart Mater. Struct.* **19**(4), 045016 (2010).
- ¹⁹Z. S. Chen, Y. M. Yang, Z. M. Lu, and Y. T. Luo, *Phys. B: Condens. Matter* **410**, 5–12 (2013).
- ²⁰A. Yang, P. Li, Y. Wen, C. Lu, X. Peng, J. Zhang, and W. He, *Appl. Phys. Expr.* **6**(12), 127101 (2013).
- ²¹S. Tol, F. L. Degertekin, and A. Erturk, *Wave Motion* **60**, 20–34 (2016).
- ²²M. Carrara, M. Cacan, M. Leamy, M. Ruzzene, and A. Erturk, *Appl. Phys. Lett.* **100**(20), 204105 (2012).
- ²³M. Carrara, M. Cacan, J. Toussaint, M. Leamy, M. Ruzzene, and A. Erturk, *Smart Mater. Struct.* **22**(6), 065004 (2013).
- ²⁴M. Carrara, J. Kulpe, S. Leadlenham, M. Leamy, and A. Erturk, *Appl. Phys. Lett.* **106**(1), 013907 (2015).
- ²⁵L. Zhao, S. C. Conlon, and F. Semperlotti, *Smart Mater. Struct.* **23**(6), 065021 (2014).
- ²⁶S. Qi, M. Oudich, Y. Li, and B. Assouar, *Appl. Phys. Lett.* **108**(26), 263501 (2016).
- ²⁷S. Tol, F. Degertekin, and A. Erturk, *Appl. Phys. Lett.* **109**(6), 063902 (2016).
- ²⁸S. Tol, F. Degertekin, and A. Erturk, *Appl. Phys. Lett.* **111**(1), 013503 (2017).
- ²⁹F. Moser, L. J. Jacobs, and J. Qu, *NDT E Int.* **32**(4), 225–234 (1999).
- ³⁰V. Giurgiutiu, *Structural Health Monitoring: With Piezoelectric Wafer Active Sensors* (Academic Press, 2007).
- ³¹M. Y. Bhuiyan, Y. Shen, and V. Giurgiutiu, *Materials* **9**(7), 602 (2016).
- ³²M. Y. Bhuiyan, J. Bao, B. Poddar, and V. Giurgiutiu, “Toward identifying crack-length-related resonances in acoustic emission waveforms for structural health monitoring applications” *Struct. Health Monit.* (in press).
- ³³Z. Liu, X. Zhang, Y. Mao, Y. Zhu, Z. Yang, C. Chan, and P. Sheng, *Science* **289**(5485), 1734–1736 (2000).
- ³⁴C. Sugino, S. Leadlenham, M. Ruzzene, and A. Erturk, *J. Appl. Phys.* **120**(13), 134501 (2016).
- ³⁵C. Sugino, Y. Xia, S. Leadlenham, M. Ruzzene, and A. Erturk, *J. Sound Vib.* **406**, 104–123 (2017).